



Extreme Wind Shear Events in US Offshore Wind Energy Areas and the Role of Induced Stratification

Mithu Debnath¹, Paula Doubrawa¹, Mike Optis¹, Patrick Hawbecker², and Nicola Bodini¹

¹National Renewable Energy Laboratory, Golden, Colorado, USA

²National Center for Atmospheric Research, Boulder, Colorado, USA

Correspondence: Mithu Debnath (mithu.debnath@nrel.gov)

Abstract. As the offshore wind industry emerges on the U.S. East Coast, a comprehensive understanding of the wind resource — particularly extreme events — is vital to the industry’s success. Such understanding has been hindered by a lack of publicly available wind profile observations in offshore wind energy areas. However, the New York State Energy Research and Development Authority (NYSERDA) recently funded the deployment of two floating lidars within two current lease areas off the coast of New Jersey. These floating lidars provide publicly available wind speed data from 20 m to 200 m height with 20-m vertical resolution. In this study, we leverage a year of these lidar data to quantify and characterize the frequent occurrence of high wind shear and low-level jet events, both of which will have considerable impact on turbine operation. We find that almost 100 independent events occur throughout the year with mean wind speed at 100 m height and power-law exponent of 16 m/s and 0.28, respectively. The events have strong seasonal variability, with the highest number of events in summer and the lowest in winter. A detailed analysis reveals that these events are enabled by an induced stable stratification when warmer air from the south flows over the colder mid-Atlantic waters, leading to a positive air-sea temperature difference.

Copyright statement. This work was authored by the National Renewable Energy Laboratory, operated by Alliance for Sustainable Energy, LLC, for the U.S. Department of Energy (DOE). The views expressed in the article do not necessarily represent the views of the DOE or the U.S. Government. The U.S. Government retains and the publisher, by accepting the article for publication, acknowledges that the U.S. Government retains a nonexclusive, paid-up, irrevocable, worldwide license to publish or reproduce the published form of this work, or allow others to do so, for U.S. Government purposes.

1 Introduction

The offshore wind industry is rapidly developing on the US east coast and a comprehensive understanding of the wind resource in this area is critical for the industry’s success. There are currently 15 active lease areas with over 21 Gigawatts (GW) of planned capacity spanning from Massachusetts to North Carolina (Fig. 1) with an additional planned 86-GW capacity in all U.S. waters by 2050 (BOEM, 2018). Proposed lease areas are located on the Atlantic Outer Continental Shelf (OCS) and span locations ranging from a minimum of 15 km to a maximum of over 100 km from the coastline. The proper planning, design, and operation of these wind farms require an in-depth understanding of the wind characteristics in the OCS, in particular the



frequency and magnitude of extreme events that largely impact the power performance, safety, and operation of wind turbines
25 (Musial and Ram, 2010; Rose et al., 2012; Archer et al., 2014).

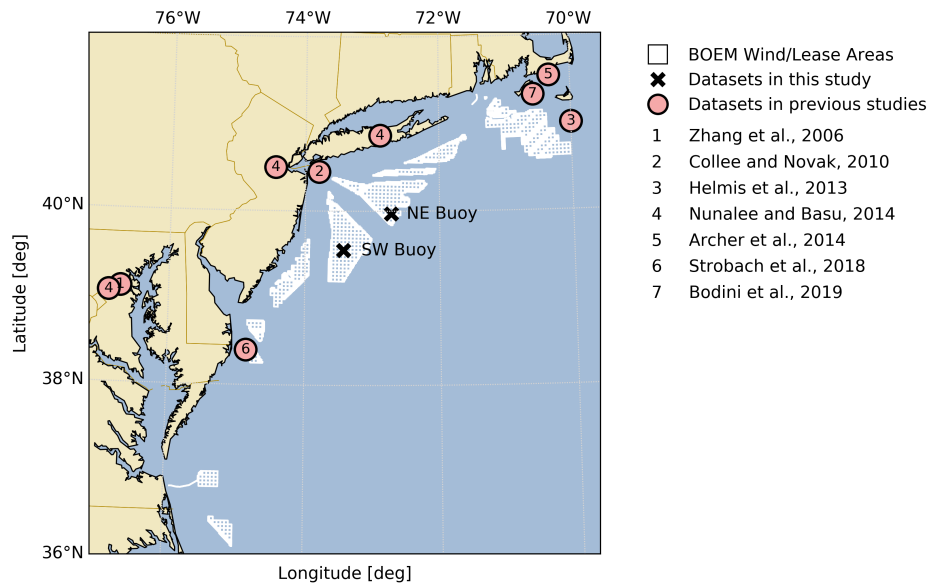


Figure 1. Map of U.S. North- and Mid-Atlantic OCS showing BOEM lease areas and wind planning areas in white (accurate as of April, 2020), the two floating lidar measurement locations (black crosses) and approximate measurement locations of previous studies focused on the offshore wind resource in this region (red circles).

Extreme wind events relevant to wind turbine operation include rapid changes in flow direction and speed, or persistently high values of shear and veer (IEC, 2019). High vertical wind shear is of particular interest to wind energy as it has a direct effect on wind turbine power and reliability (Murphy et al., 2019; Gutierrez et al., 2014, 2017, 2019; Colle and Novak, 2010). In the last decade, a growing body of work has identified and characterized high-shear events in the U.S. Mid-Atlantic that are brought on by low-level jets (LLJs). These offshore LLJs, spanning from Maryland to New Jersey, have been investigated with the Weather Research and Forecasting (WRF) model (Strobach et al., 2018; Colle et al., 2016; Nunalee and Basu, 2014), ship-borne lidar (Pichugina et al., 2017; Strobach et al., 2018), aircraft measurements (Colle et al., 2016), sodar (Helmis et al., 2013), radiosonde (Helmis et al., 2013; Colle and Novak, 2010; Nunalee and Basu, 2014), and radar wind profilers (Zhang et al., 2006; Nunalee and Basu, 2014). A consensus agreement among these studies is the frequent occurrence of persistent
30 LLJs in this area during the warm season. While some studies were limited to heights above wind turbine operation (Nunalee and Basu, 2014; Zhang et al., 2006), others found wind speed maxima at heights representative of a typical wind turbine rotor
35 (Pichugina et al., 2017; Strobach et al., 2018; Colle and Novak, 2010).

These previous studies have found the development of LLJs in the Mid Atlantic to be strongly linked to static stability in the atmospheric boundary layer (ABL). Despite the importance of stratification to this and other wind phenomena, there is still a
40 lack of consensus on what may be the prevailing conditions of stability and turbulence in this region. Analyses of near-shore



measurements have indicated both very low turbulence conditions (Bodini et al., 2019), indicative of stable stratification, and predominantly unstable conditions (Archer et al., 2016). Given the role of atmospheric stability in influencing wind profiles across the nominal rotor layer as well as turbine wake propagation, it is clear that more analysis and data are needed to better understand prevailing atmospheric conditions in the Atlantic OCS.

45 While the aforementioned studies were extremely valuable in providing an initial characterization of offshore wind conditions, limitations of the measurements used undermine their value to current US east coast wind energy lease areas. Many of the datasets were spatially disjunct (Pichugina et al., 2017; Strobach et al., 2018; Colle et al., 2016) or limited to coastal areas (Colle et al., 2016; Helmis et al., 2013; Nunalee and Basu, 2014; Zhang et al., 2006). The only two experiments recorded in literature that were far enough from the coast to be representative of conditions that will be experienced by offshore wind plants
50 were limited in duration to a maximum of one month (Helmis et al., 2013; Strobach et al., 2018; Pichugina et al., 2017).

Increasing investments in offshore wind energy along with continuous instrumentation developments have enabled a surge in deployments of offshore wind measurement systems. In particular, the emergence of buoy-mounted floating lidar has led to at least 10 and as many as 20 floating lidar deployments in the US east coast in recent years. At large, these data have been kept proprietary and any derived analyses have not been disseminated. In August and September 2019, however, the New
55 York State Energy Research and Development Authority (NYSERDA) funded the deployment of two floating lidars (DNVGL, 2020) within two current lease areas in the New Jersey offshore wind area (Fig. 1). These floating lidars provide wind data at multiple heights across the rotor layer (Table 1). To our knowledge, these deployments provide the first publicly available comprehensive and relevant data set for the analysis of wind characteristics in US east coast active lease areas and, as such, are of immense value for wind energy research.

60 A cursory look at the NYSERDA data alone can reveal very important wind characteristics and phenomena. We show an example of this in Fig. 2 where an intense high-shear event existing over a 2-day period is measured at the northeast (NE) buoy. Not only do we see frequent extreme shear across the nominal rotor area but also several very-low-level jet (VLLJ) events where the peak in the wind profiles is as low as 100 m. In the highlighted VLLJ and monotonic-shear periods, the time-averaged profiles reveal a power-law exponent of 0.59 and 0.32, respectively, when measured across a nominal rotor
65 layer spanning between 40 m and 160 m. This corresponds to wind speed gradient, $\Delta U/\Delta z$, values of 0.12 1/s and 0.08 1/s, respectively, across the rotor layer. The ability to accurately predict such events using numerical weather prediction (NWP) models is crucial for wind resource assessment, wind power forecasting, and for the timely implementation of operation and maintenance procedures to protect turbines from damage. A proper documentation of these extreme events will help to identify the shortcomings of the models needed for further improvement and also will guide the development of more accurate standard
70 guidelines for offshore wind turbines. To our knowledge, the existence of these high-shear events, let alone their causes and development, have not been previously studied in the US east coast offshore wind lease areas. Our goal is to characterize these events and understand the physical mechanisms governing their onset and dissipation. To do so, we leverage these novel floating lidar observations in the US offshore wind areas.

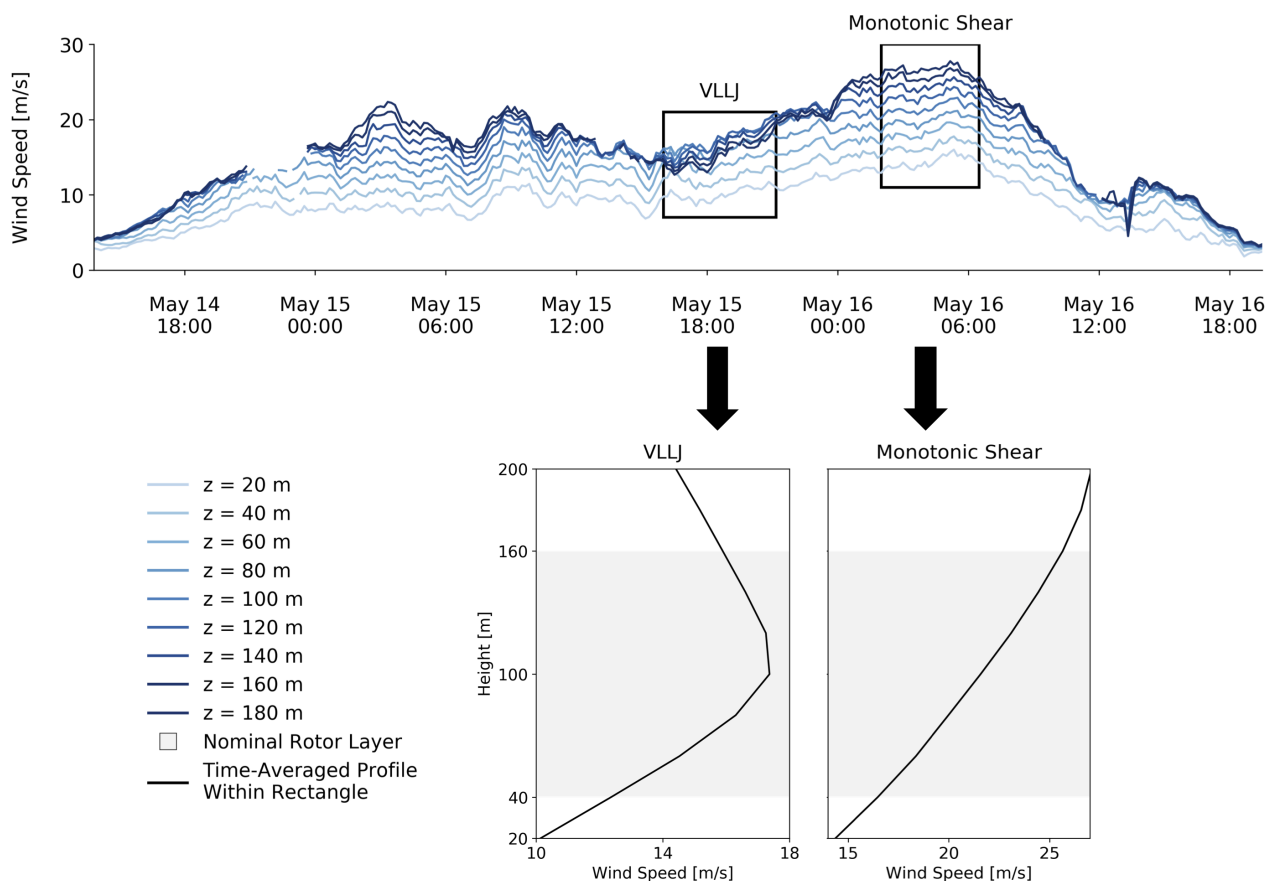


Figure 2. Example of high-shear event as measured by lidar on NE buoy. Time series between May 14 2020, 13:50 UTC and May 16 2020, 19:30 UTC (top). The data within the two black boxes are time-averaged and shown below the timeseries as examples of very-low-level jet (VLLJ) and monotonic-shear periods.

Table 1. Summary of dataset being analyzed: site name, location (latitude, longitude), period analyzed, distance from coast due West, lidar measurement heights (above mean sea level), and quantities being analyzed.

Site Name	Location	Period Analyzed	Distance from Coast	Lidar Measurement Heights	Quantities Analyzed
SW Buoy	39.55°N, 73.43°W	Sep 4, 2019 - Aug 16, 2020	~ 69 km	20 m-200 m	Wind speed and direction, turbulence intensity,
NE Buoy	39.97°N, 72.72°W	Aug 12, 2019 - Aug 16, 2020	~ 114 km	every 20 m	2-m air temperature, sea surface temperature



2 Identification of High-Shear Events

75 Time series of vertical profiles of wind speed at the two buoy sites are used to detect and characterize high-shear events that are relevant for offshore wind development. The algorithm developed to detect these events discerns between two types of wind speed profiles: monotonic shear and VLLJ (Fig. 2). The algorithm is applied to each 10-minute-mean profile. When high shear is detected for a continuous period of one hour or longer, this period is defined as a high-shear event. To avoid double counting, separate events that are close in time and measured at the same site are merged into a single, longer event. This is done in
 80 two steps: first, events with lower shear that last one hour or less but are sandwiched in between two high-shear periods are identified as integral part of the adjacent events and merged into them to form one, longer event; finally, two events that are within six hours of each other are merged into a single, long-lived event.

The monotonic-shear profiles refer to 10-minute averaged profiles in which the wind speed magnitude strictly increases with height (Fig. 2, right-side profile). For the VLLJ cases, the wind speed magnitude increases up to a certain height and then
 85 decreases, revealing the presence of a LLJ with a nose below 200 m (Fig. 2, left-side profile). While the monotonic shear cases could be the lower part of a LLJ with a nose above 200 m, the vertical extent of our measurements does not allow for that distinction to be made. For this reason, the algorithm was developed to distinguish between both.

The detection of both types of high-shear profiles is based on several conditions, as outlined below and shown by the schematic in Fig. 3. We define nominal hub height and rotor diameter values to be 100 m and 120 m, respectively (the rotor
 90 span being between 40 m and 160 m). These are assumed to be representative of an offshore wind turbine and are used here to facilitate the interpretation of results in the context of offshore wind development. For the analysis performed here, only profiles with a hub-height wind speed greater than 3 m/s are considered. A profile is classified as “monotonic shear” if

- (i) the rotor-layer shear is greater than a pre-specified threshold value,

$$\left. \frac{\Delta U}{\Delta z} \right|_{\text{rotor}} \geq \left. \frac{\Delta U}{\Delta z} \right|_{\text{rotor_threshold}}$$

95 A profile is classified as “VLLJ” if

- (i) the height of maximum shear (as computed between $z_{\text{rotor_bottom}}$ and z) is between the second (40 m) and second-to-last (180 m) measurement height,

$$40 \leq z \left(\left. \frac{\Delta U}{\Delta z} \right|_{\text{max}} \right) \leq 180;$$

- (ii) the maximum shear across the rotor layer is greater than the same pre-specified threshold value used for the monotonic-shear detection,

100

$$\left. \frac{\Delta U}{\Delta z} \right|_{\text{rotor,max}} \geq \left. \frac{\Delta U}{\Delta z} \right|_{\text{rotor_threshold}} \quad ; \text{ and}$$

- (iii) the wind speed drop off above the jet nose meets minimum requirements in terms of dimensional and dimensionless threshold values,

$$\Delta U_{\text{drop}} \geq 1.5 \text{ m/s and } \frac{\Delta U_{\text{drop}}}{U_{\text{nose}}} \geq 10\%$$

105 where $\Delta U_{drop} = U_{top} - U_{nose}$ and U_{top} marks the top of the jet and is the first local minimum in wind speed identified above the nose. The enforcement of both dimensional and nondimensional wind speed drop off criteria is based on previous work (Baas et al., 2009) but the threshold values are adjusted in magnitude here due to the limited vertical extent of the measurement data available.

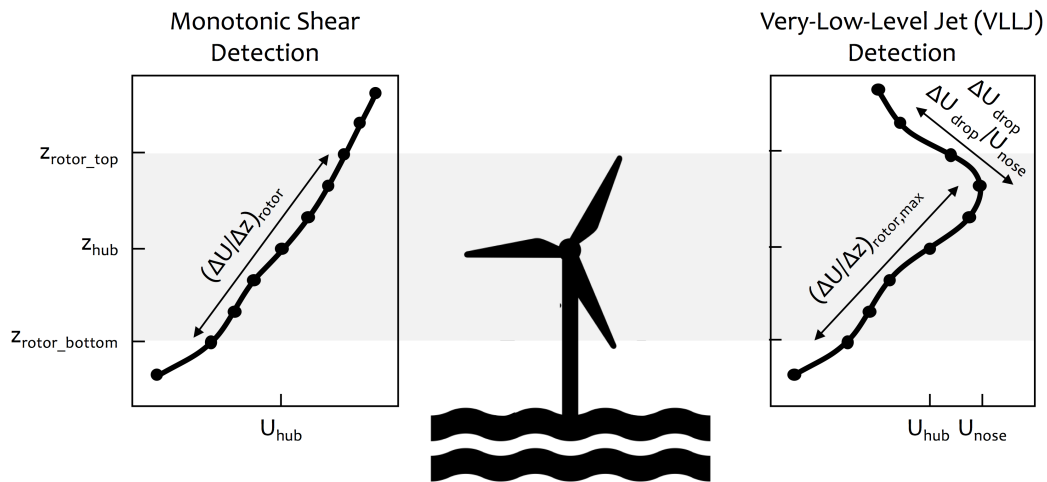


Figure 3. Schematic showing key quantities used in the algorithm developed to detect the two types of high-shear profiles considered herein: monotonic shear and very-low-level jet (VLLJ). Individual detections are then merged into events.

In the wind energy industry, the vertical wind shear is typically represented by the power-law exponent, α (IEC, 2019).
 110 However, in this work, the variable used to quantify vertical wind shear is wind speed gradient between a reference height (here taken as 40 m) and other heights above it. A relationship plot (Fig. 4a) among wind speed at hub height, U_{100m} , wind speed gradient across the rotor, $\frac{\Delta U}{\Delta z}$, and shear exponent, α , explains that the shear exponent can be very low even though a turbine faces high wind speed difference across its diameter. The shear exponent is non-dimensional and does not consider the magnitude of wind speed that a turbine actually faces. As a result, data points that would normally be considered as high shear
 115 by α often have relatively low wind speeds and would not pose a danger to wind turbines. To better capture events that do pose that danger, we consider instead the $\frac{\Delta U}{\Delta z}$ metric — which does account for wind speed magnitude — as a threshold for detecting high wind shear events. The distribution of $\frac{\Delta U}{\Delta z}$ for the buoys are presented in Fig. 4b. The figure shows a long tail in the the distribution that captures a considerable number of high shear events. Setting a threshold at the 90th percentile, as shown in the figure, is able to capture a large number of events while still ensuring that the shear values are extreme. Herein,
 120 for both types of profiles, the threshold shear value $\frac{\Delta U}{\Delta z} \Big|_{rotor_threshold}$ is set to the 90th percentile of the distribution of $\frac{\Delta U}{\Delta z} \Big|_{rotor}$ over the entire measurement period, which equals 0.035 s^{-1} (Fig. 4b) when averaged across the lidars.

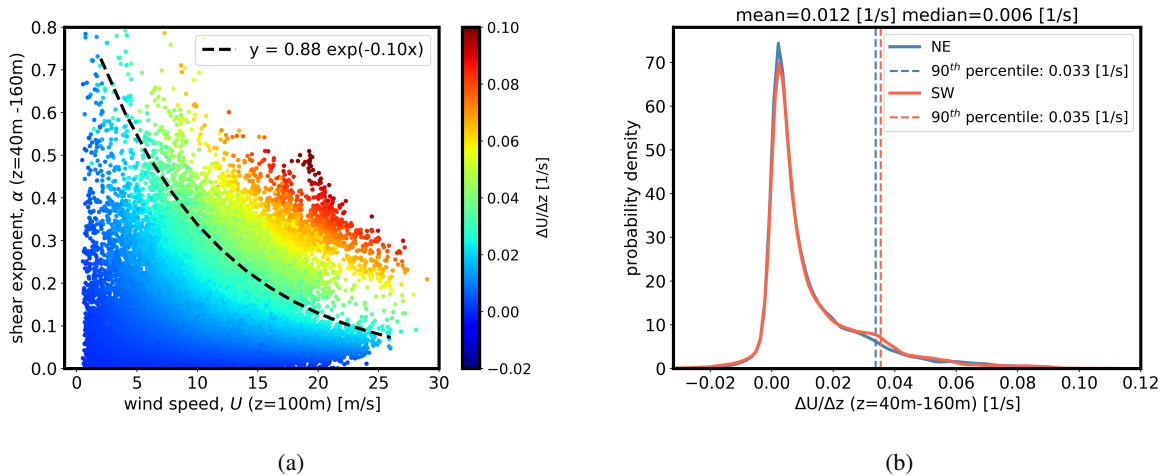


Figure 4. An analysis of vertical wind shear parameters from the NE floating lidar. Panel (a) shows the relationship between the wind speed at 100 m height (U_{100m}), the power-law exponent between height 40 m and 160 m (α), and the wind speed gradient between 40 m and 160 m ($\Delta U/\Delta z$). The black dashed line represents the 90th percentile value of $\Delta U/\Delta z$. Panel (b) shows the probability distribution of $\Delta U/\Delta z$ for both buoys.

3 Results

3.1 Detected Events

We first summarize the results of the high-shear detection algorithm in Fig. 5. A large number of events are detected at both
 125 lidars, most of which are less than 10 hours but some which extend for more than two days. All the events identified based on
 the detection criteria are marked as "high shear" events and presented in this section and include both VLLJ and monotonic-
 shear cases. The total number of detected events are 104 and 92 for Northeast (NE) and Southwest (SW) buoy, respectively.
 To explain why there are more events at the SW buoy, we must first better understand the atmospheric conditions in which
 these events are able to occur. We begin this investigation in the next section by looking at seasonal and diurnal trends in event
 130 frequency.

3.2 Seasonal and Diurnal Dependence

We explore seasonal and diurnal trends in the high-shear events in Fig. 6. In Fig. 6a & Fig. 6b, we consider the number of
 10-minute average data points as they depend on hours of diurnal cycles and months, respectively. In Fig. 6c, we consider
 actual event counts by month. We see in Fig. 6a a clear diurnal trend in the high-shear events, with event frequency increasing
 135 after noon and dropping after 22:00. Indeed, events are twice as likely to happen during the night than during the morning. We
 see in Fig. 6b and Fig. 6c that there is also a strong seasonal trend in event frequency. Events are largely concentrated in the

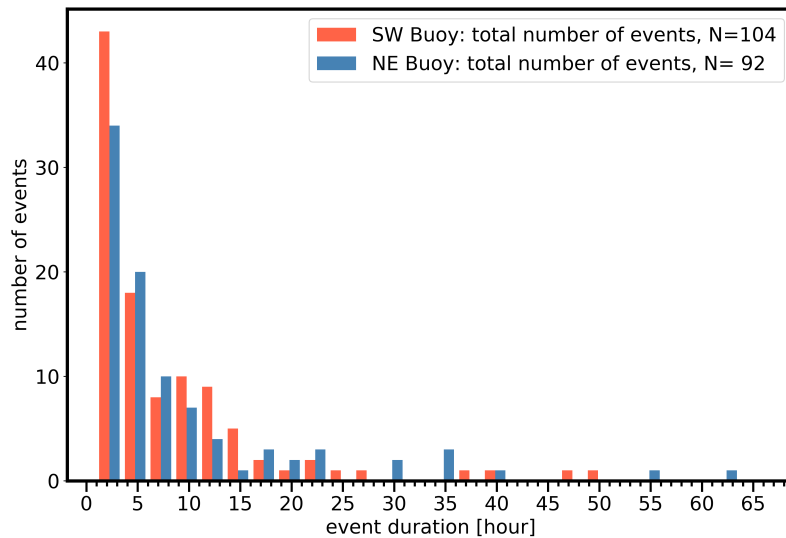


Figure 5. Number of high shear events for both buoys as a function of event duration. Only events with minimum duration of 1 hour are considered.

spring months (i.e., March through June) and are much less frequent in the rest of the year. In particular, the month of June has the highest number of events (16 events, on average) and November has the lowest number of events (on average 1 event).

The presence of strong diurnal and seasonal trends in the number of high-shear events suggest the influence of local meteorological conditions, particularly, the atmospheric stability. Indeed, we expect this to be the case which follows the well-established relationships between high wind shear, LLJs and thermodynamic atmospheric stability established by previous works (Monin and Obukhov, 2009; Stull, 1988; Poulos et al., 2002; Wharton and Lundquist, 2012). In the next section, we explore this possible relationship between high shear and atmospheric stability in more detail.

3.3 Atmospheric Stability and Turbulence

In this section we explore the role of atmospheric stability and turbulence in driving these high-shear events. To measure atmospheric stability, we are limited to quantifying the difference in 2-m air temperature, T_a , and the sea surface temperature, SST , given the lack of temperature measurements aloft. We denote this air-sea temperature difference as ΔT from herein. To measure turbulence, we use the turbulence intensity (TI) measurements at 100 m as measured by the floating lidars, denoted TI_{100m} . In Fig. 7a & Fig. 7b, we plot distributions of ΔT and TI_{100m} , where the full data set are shown in blue with the high-shear events shown in orange.

It is clear from Fig. 7a that high-shear events are strongly associated with a positive air-sea temperature difference ($\Delta T > 0$). The distribution of TI_{100m} is shown for both high-shear events and the full data set in Fig. 7b. The high shear events have

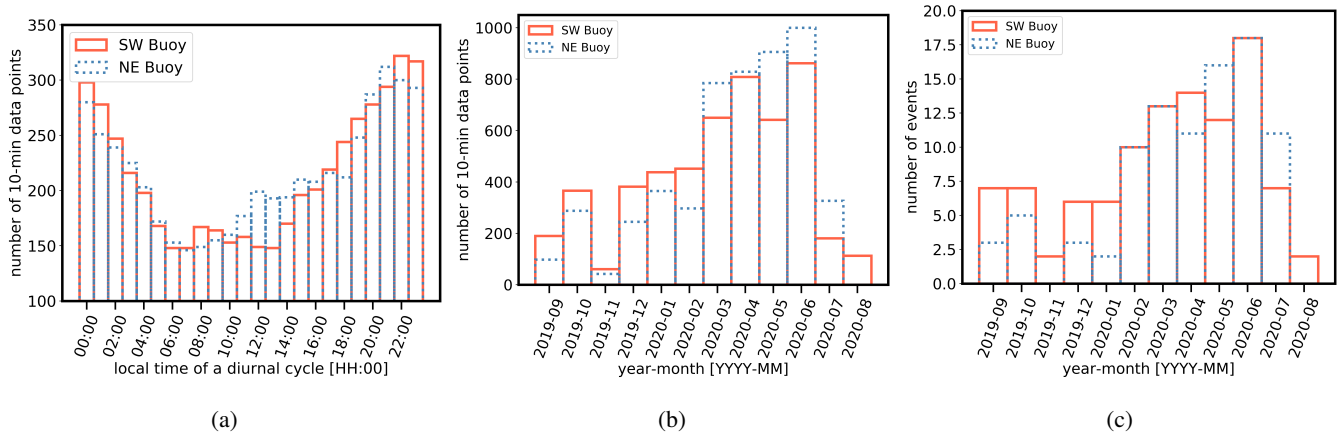


Figure 6. Diurnal and seasonal distribution of high-shear events at both buoys: number of 10-min profiles in which high shear was detected as a function of local time (a) and month (b), and number of events across the year (c).

turbulence intensity mostly within the bin of 4% to 6% (mean TI_{100m} , 5.1%) whereas mean turbulence intensity of all the data-set is 8.3%. Focusing only on the high-shear events (i.e., the orange distributions), we plot ΔT and TI distributions by wind direction in Fig. 7c and Fig. 7d. We see that these high-shear events are almost exclusively associated with southwesterly flow with a mean wind direction of 217° . Referring to Fig. 1, we see that southwesterly flow is about parallel to the coastline and features an area of very large ocean fetch.

The observations in Section 3.3 suggest the role of induced stable stratification in causing these high-shear events. It is possible that warmer air coming from the southwest encounters the colder waters of the Mid-Atlantic, causing a positive air-sea temperature difference. This temperature difference would then induce stable stratification where vertical turbulent exchange from surface winds to those aloft would be reduced and a degree of “decoupling” of winds aloft from the surface would occur. Combined with the long ocean fetch where surface roughness is low, this is likely leading to very low turbulence in the winds aloft at the floating lidars, sufficient to cause high wind shear and allow for the formation of low-level jets.

We provide evidence of this induced stratification in Fig. 8 for two high-shear events. As shown for both case studies, the onset of high shear aligns with the switch from a negative ΔT to a positive ΔT value. Notably, the end of the second high shear event aligns with the switch back to a negative ΔT value. Furthermore, we see that the change in sign in ΔT is driven by changes in the air temperature, T_a , while the SST remains relatively constant before, during, and after the high shear events. So indeed, the arrival of warm air from the southwest and the resulting induction of stable stratification appears to be a dominant contributor to these high-shear events.

We further examine the role of the air-sea temperature difference in influencing wind conditions in Fig. 9. Here we consider the full set of data and not just the high-shear events, Specifically, we show the relationship between ΔT and wind speed at 100 m, TI at 100 m, the shear exponent, α , across the rotor layer, and the maximum wind speed gradient across the rotor, $\Delta U / \Delta z_{max}$. The data are bin-averaged and shown along with the standard deviation within the bin. The density of the data

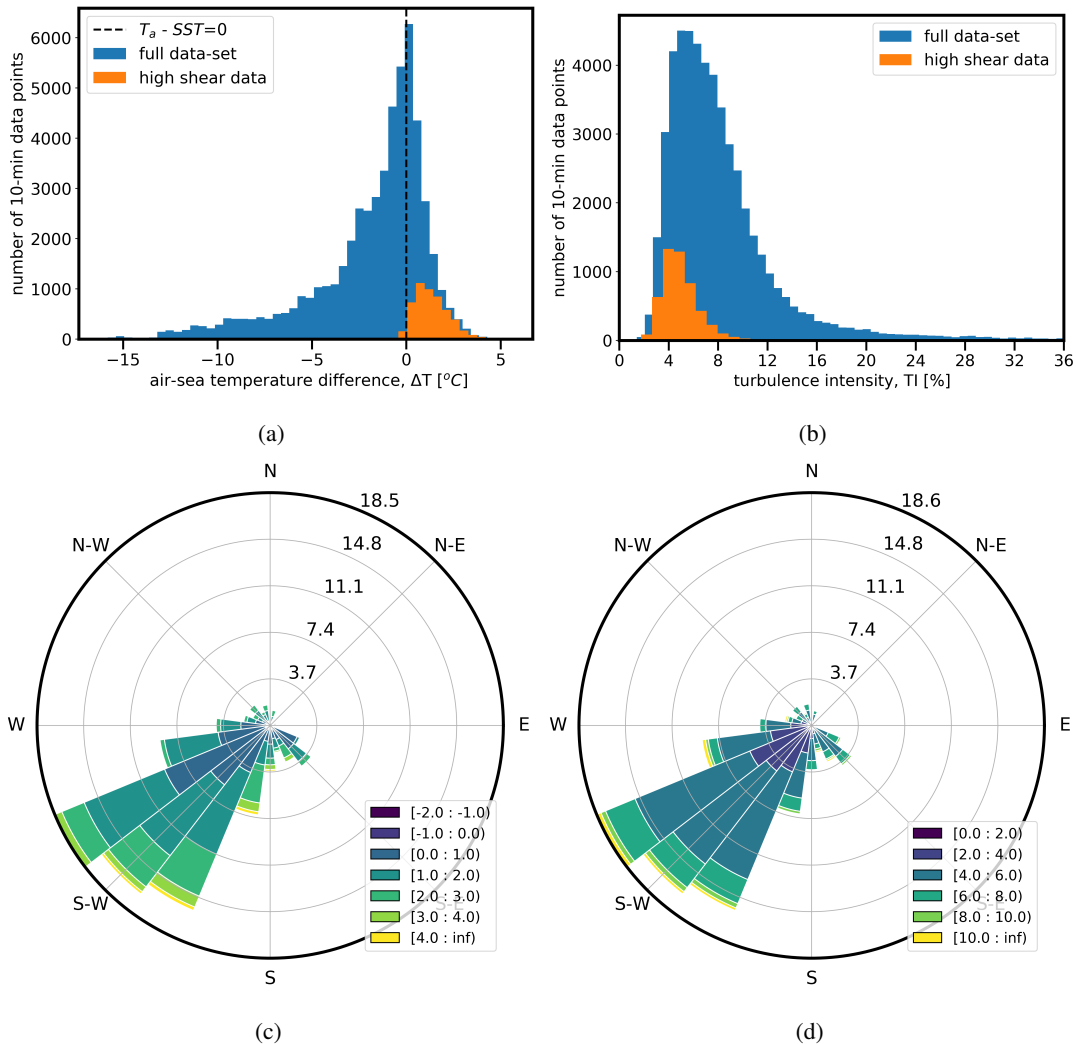


Figure 7. Dependency of high shear events on air-sea temperature difference (a, c) and turbulence intensity (b, d). Top figures show distribution for entire data set vs. periods in which high shear was detected. Bottom figures show distribution roses for high-shear periods only. Data are shown for NE buoy only.

is shown with red color in the background. We see that wind speed at hub height is almost constant when the temperature difference is negative, but increases sharply when temperature difference is positive. The linear increase of wind speed with increase of positive temperature difference ($\Delta T > 0$) suggests that the strength of extreme events is highly dependent on the magnitude of positive temperature difference. On the other hand, turbulence intensity at hub height drops as the temperature difference approaches zero, showing a strong dependency on static stability (Fig. 9b). There is an upward trend in the turbulence intensity after $\Delta T = 2$ °C. This could be due to a low density of the data within the bin. Similar to wind speed, both the shear

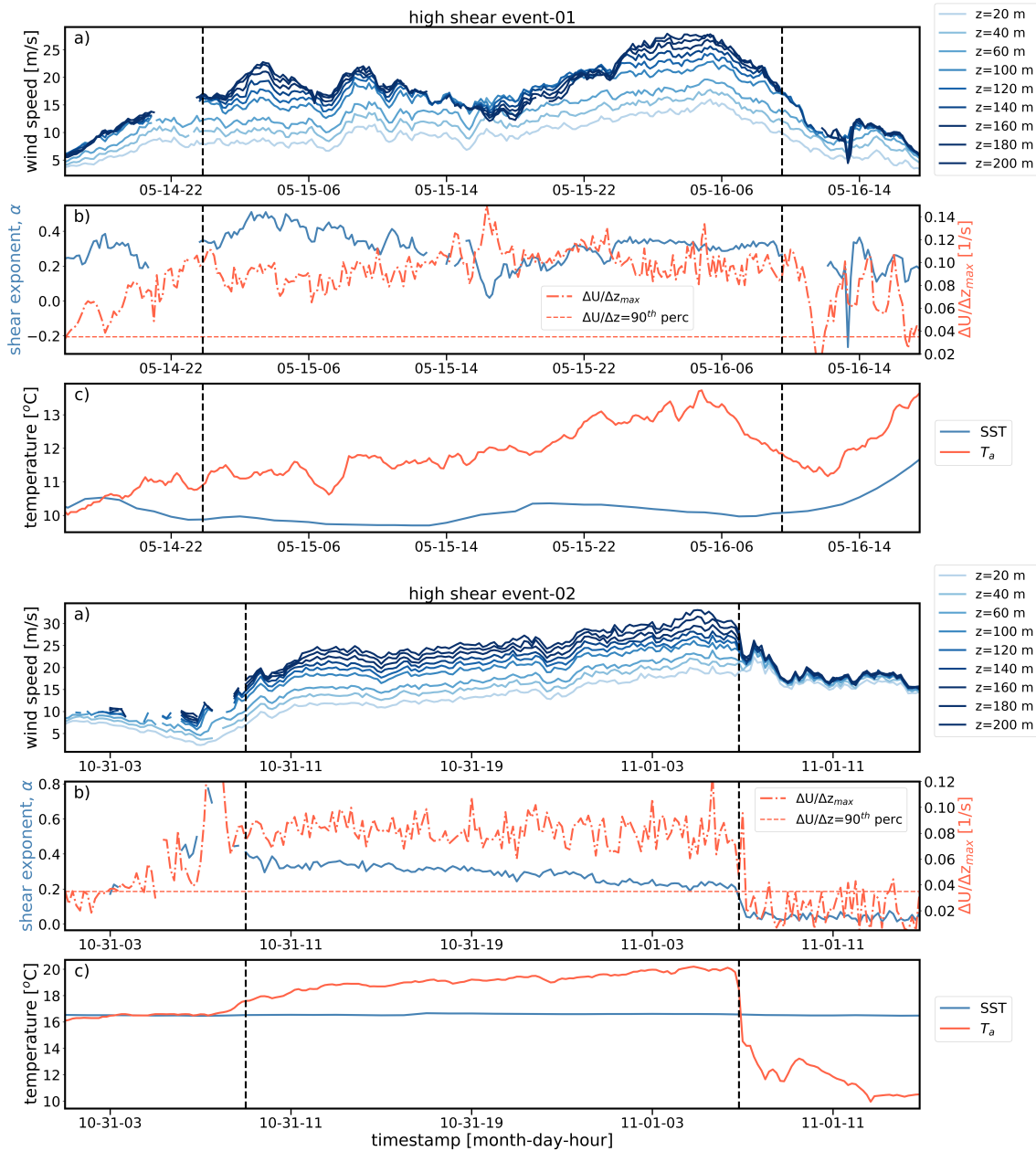


Figure 8. Two examples of high-shear events measured at NE buoy. Subfigures show time series of wind speed, wind shear (power-law exponent α) and wind speed gradient ($\Delta U/\Delta z_{max}$), air (T_a) and sea surface temperature (SST). Vertical dashed lines represent start and end time of the high shear events.

180 exponent (Fig. 9c) and the maximum wind shear (Fig. 9c) are roughly constant when ΔT is negative before increasing sharply when the difference becomes positive.

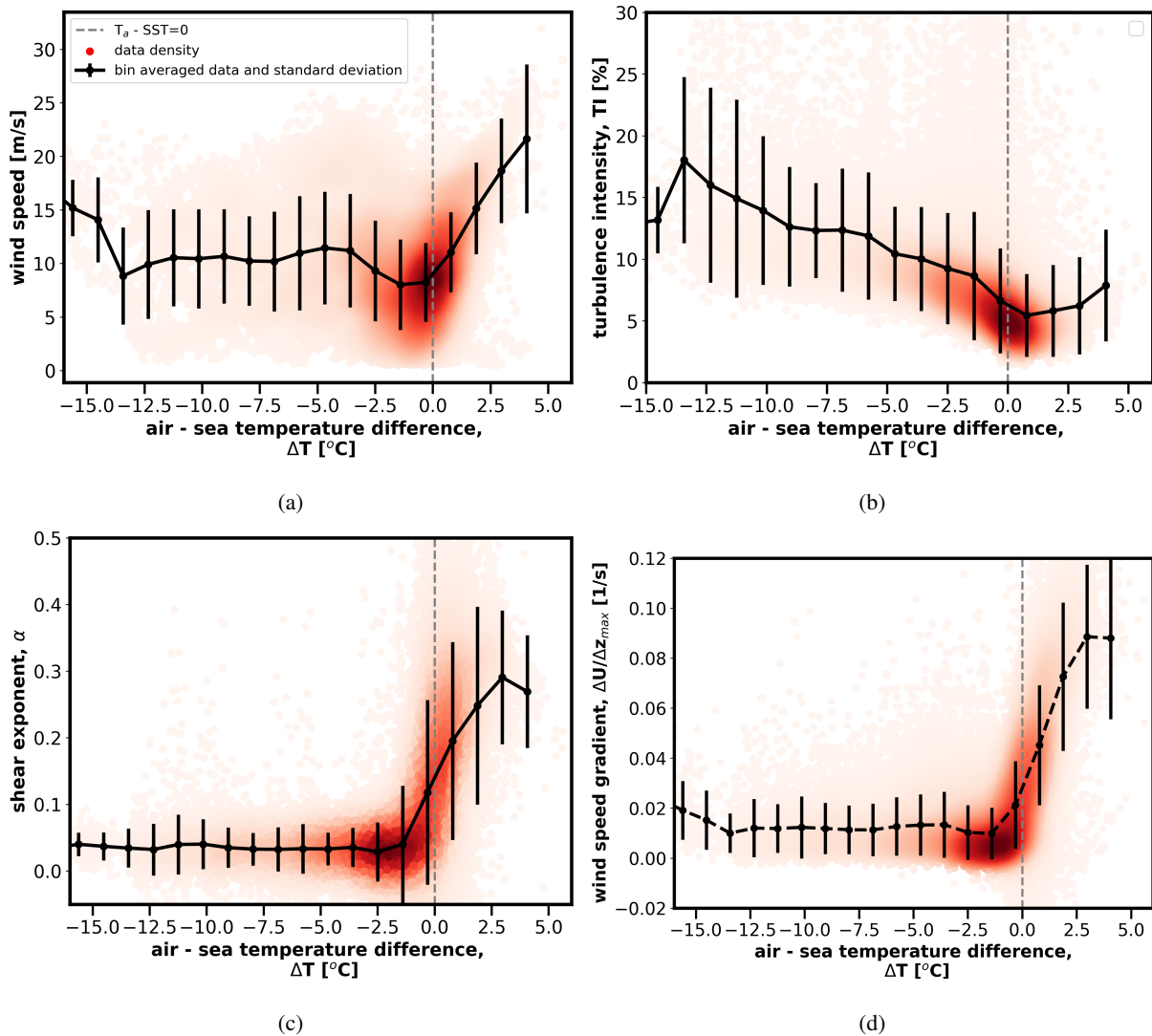


Figure 9. Wind characteristics as they depend on the air-sea temperature difference. Only NE buoy data are shown here. a) wind speed; b) turbulence intensity; c) wind shear exponent; d) maximum wind speed gradient across the nominal rotor defined here (between 40 m and 160 m).

3.4 Spatial Variability

In this section we briefly explore potential reasons for 13% more events being observed at the SW buoy. In Table 2 we show a comparison of mean atmospheric variables between the two buoys, both for the high-shear cases and for the full data set. To perform a proper inter-comparison between the buoys, timestamps that are common for both buoys are only considered.



We see in Table 2 that the local air temperature at the NE buoy is lower than the SW buoy. Furthermore, the change of air temperature between the buoys, $T_{a,SW} - T_{a,NE}$, is higher than the change of SST between the buoys, $SST_{SW} - SST_{NE}$. Therefore, the lower air temperature at the NE buoy is largely responsible for its lower air-sea temperature difference relative to the SW buoy. This higher air-sea temperature difference at the SW buoy corresponds to notably lower TI and a slightly higher wind speed gradient across the rotor relative to the NE buoy, although the latter difference is small and could be within the measurement uncertainty.

Table 2. Comparison of the mean atmospheric variables between the NE and SW buoys.

Variables [units]	High shear data			All the data		
	SW buoy	NE buoy	SW buoy - NE buoy	SW buoy	NE buoy	SW buoy - NE buoy
T_a [$^{\circ}C$]	13.967	13.615	0.352	13.014	12.668	0.3459
SST [$^{\circ}C$]	12.446	12.212	0.234	14.582	14.604	-0.023
$T_a - SST$ [$^{\circ}C$]	1.521	1.404	0.117	-1.621	-1.936	0.3147
α []	0.286	0.289	-0.003	0.103	0.097	0.0066
$\Delta U / \Delta z$ [1/s]	0.050	0.0491	0.0010	0.0127	0.0123	0.0004
$\Delta U / \Delta z_{max}$ [1/s]	0.0753	0.0731	0.0022	0.0250	0.0245	0.0005
U_{100m} [m/s]	16.179	15.735	0.445	9.843	10.116	-0.2736
TI_{100m} [%]	4.379	5.119	-0.740	7.833	8.327	-0.4930

3.5 Very Low-Level Jets

Up to this point, the analysis considered high-shear events irrespective of the profile characteristics across a nominal rotor span. Here, we focus on a subset of 10-minute periods that are interspersed within these high-shear events: those with a VLLJ. These events are of particular interest to wind energy applications as they subject the rotor not only to high shear, but also to negative shear when the jet nose is within the rotor span.

Out of the 104 (92) high-shear events detected for the SW (NE) buoy, 30% (26%) feature VLLJs and 9% (7%) are made up entirely of VLLJ profiles. These profiles were not detected at any specific point of the high-shear events. Instead, they occurred at the beginning, end, and throughout the longer-lived events. A simple statistical analysis of these VLLJ profiles confirms that they are highly relevant for wind turbine operation: the most common nose wind speeds are between 9 m/s and 12 m/s, and the most common nose heights 80 m and 100 m. As expected, the predominant wind direction during these VLLJ occurrences is consistent with that for the long-lived, high-shear events: primarily from the SW sector. These VLLJs exhibit a clear seasonal signature, being most frequently in spring and not occurring at all in winter (Fig. 11a). No clear diurnal signature can be identified (Fig. 11b), as is expected for the offshore environment where diurnal fluctuations are less pronounced than in land.

The highest shear values seen throughout this year of measurements correspond to VLLJ profiles, as evidenced by the pronounced tail of the VLLJ maximum-shear distributions in Fig. 12a. When the nose of the jet is within the rotor swept area, a portion of the rotor will experience negative shear. Here, we quantify how much of the rotor experiences negative vs. positive

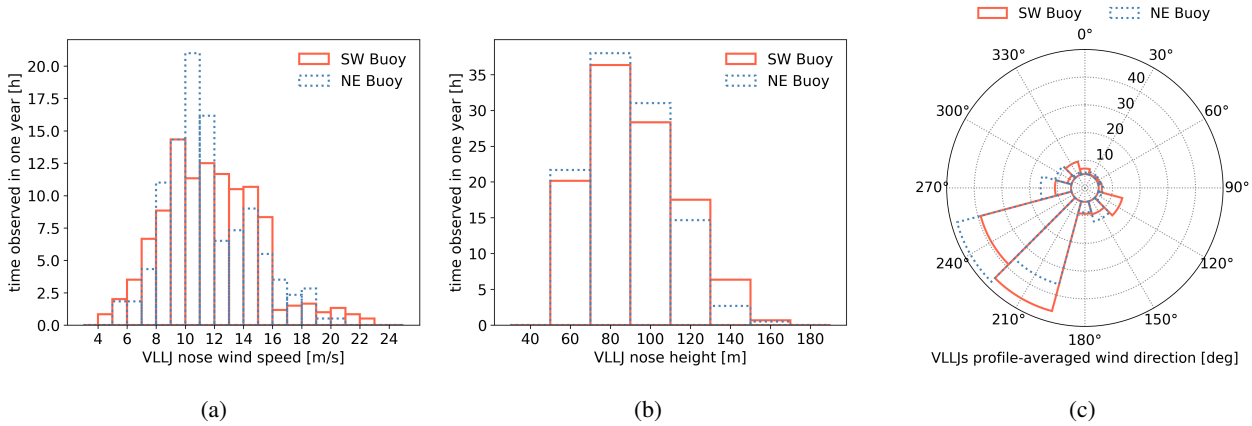


Figure 10. Number of hours of VLLJ as a function of nose wind speed (a), nose height (b), and vertically averaged wind direction (c). Distributions consider all 10-minute profiles featuring a VLLJ.

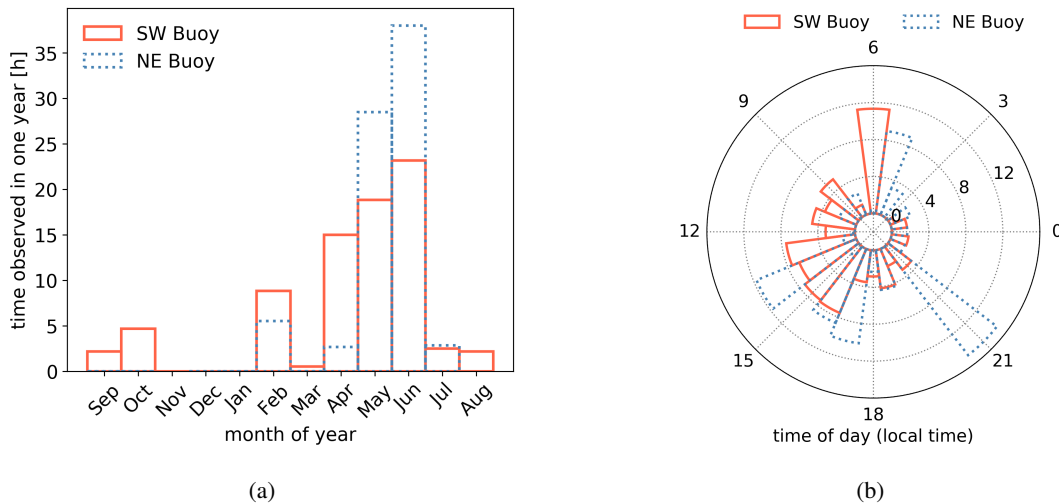


Figure 11. Number of hours (over the entire year) in which VLLJs were observed at both buoys as a function of month (a) and time of day (b). Distributions consider all 10-minute profiles featuring a VLLJ.

shear for each VLLJ profile using the turbine-jet relative distance parameter [ξ , Gutierrez et al. (2017, 2019)]. These values are shown in Fig. 12b: -1 indicates entirely positive shear across the rotor, 0 half negative and half positive, and 1 entirely negative.

210 This analysis reveals that the nominal rotor defined here experiences at least some negative shear during most of the VLLJ profiles identified: less than 1% of VLLJs have $\xi = -1$. More than 50% of the VLLJ profiles identified have more negative than positive shear across the rotor ($1 > \xi > 0$). While the mean negative shear is not too high (i.e., $\Delta U/\Delta z = -0.024 \text{ s}^{-1}$ for both buoys), the distribution reveals a noticeable tail where $\Delta U/\Delta z < -0.035 \text{ s}^{-1}$ (Fig. 12c). While previous work (Gutierrez

et al., 2017) has found that negative shear can decrease loads on the wind turbine system (primarily at the nacelle and tower),
 215 the positive shear in these profiles has been directly linked to an increase in static and dynamic loads relative to a well-mixed
 profile (Gutierrez et al., 2016). A recent study (Gutierrez et al. (2019)) investigated the symmetry in wind turbine loads when
 the rotor experiences half positive, half negative shear and found complex interplay between the tower, blades, and gravitational
 loads. The complexity of this aero-structural problem and the nature of these boundary layer profiles off the U.S. east coast
 highlight that more studies are needed to support the successful deployment of offshore wind turbines in the U.S.

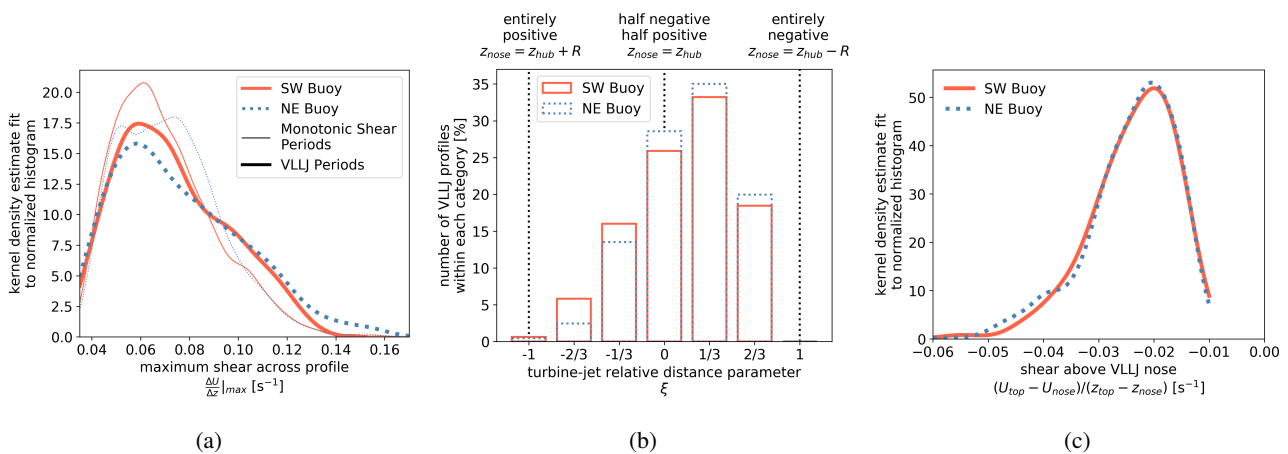


Figure 12. Distribution of maximum shear over one year of measured profiles and separated by profile type: monotonic vs. VLLJ (a); distribution of turbine-jet relative distance parameter for all VLLJ profiles (b); distribution of shear above VLLJ nose (between nose and local wind speed minimum measured above it), shown only for 10-minute periods with VLLJ profile (c).

220 The high-shear periods measured at the two sites had substantially lower turbulence levels than the remainder of the data.
 This is exemplified in Fig. 13 where TI is given as a function of wind speed for all 10-minute periods without a high-shear
 profile (black) and those with a VLLJ profile (colors). Note that the monotonic shear profiles are not included here, but their
 turbulence distribution is similar than that of the VLLJ profiles. As expected, most of the data (the profiles not flagged as
 having high shear) follows a decreasing trend with wind speed up to a certain point, and then sees a slight increase as wind
 225 speeds go up again and generate mechanical turbulence. For example, the SW buoy goes from 5.9% TI at 8 m/s to 7.8% TI at
 20 m/s. The same is not seen for the VLLJ-exclusive data: a TI value of 4.9% at 8 m/s decreases even further as the wind speed
 increases, to about 3.7% at 20 m/s. This is likely due to the surface-layer high shear: the wind speed increase at hub height does
 not necessarily translate to an equally large wind speed increase near the ocean surface. These low values of turbulence also
 suggest stable atmospheric stratification, which has been found to support LLJ formation not only on land but near the shore
 230 in the U.S. eastern coast Colle and Novak (2010).

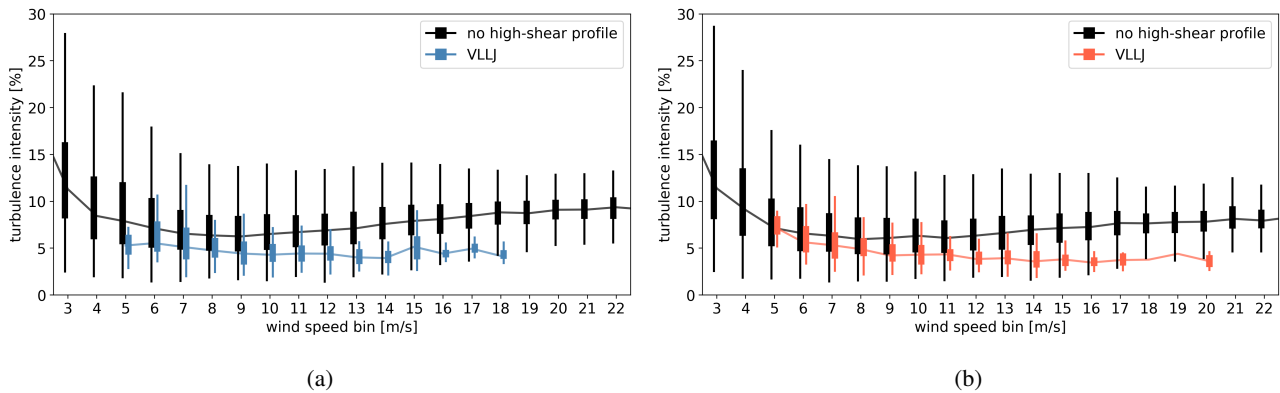


Figure 13. Hub-height ($z = 100$ m) distribution of turbulence intensity for wind speed bins between 3 and 22 m/s for NE (a) and SW (b) buoys. Distributions are shown separately for all 10-min periods without a high-shear profile (black) and those with a VLLJ profile (colored). Only wind speed bins with at least ten VLLJ profiles are shown. Monotonic shear periods are excluded here for clarity.

4 Synoptic Overview

Our analysis to this point has demonstrated the frequency of extreme high-shear events that are caused by stable stratification induced by warmer air from the southwest flowing over colder mid-Atlantic waters. In this section, we examine the synoptic conditions that lead to the arrival of warmer southwest air.

235 Synoptic conditions during these high shear events generally consist of a surface low pressure system centered west of the floating lidar locations and a region of high pressure to the east as depicted in Fig. 14a. The exact location of these pressure systems deviates from case to case but the general pattern holds resulting in a large southerly component to the near surface winds. The directional component of the wind speeds is an important feature as winds coming from the south typically results in warmer air being advected into the area. Additionally, winds with a southwesterly component may be coming from onshore
240 and can contain much higher air temperatures due to stronger heating over land during the day. Further, the long fetch over the ocean results in low turbulent conditions.

Of the 86 days that registered an event, nearly 75% were observed to have this general synoptic set up. This synoptic setup has been seen in previous studies pertaining to offshore low-level jets in the mid-Atlantic region such as Zhang et al. (2006), Colle and Novak (2010), Helmis et al. (2013), and Strobach et al. (2018). While these studies each provide different
245 mechanisms for the low-level jet formation, the synoptic setups are generally consistent with each other. In most cases, the cyclone to the west advances towards the east or northeast denoted by the blue arrow in Fig. 14a.

Many of the stronger events coincide with the western low pressure system strengthening and moving eastward as the pressure gradient ahead of the cold front tightens and increases the wind speeds over the floating lidars (see Fig. 14b). Of the 10 longest events (averaging 30 hours in duration), 7 exhibited a tightening of the gradient and increase in wind speed as the
250 event progressed. Helmis et al. (2013) and Strobach et al. (2018) found a similar tightening of the pressure gradient during cases of offshore low-level jets in the mid-Atlantic resulting in a strengthening of the wind speeds and shifting of the winds to contain



a stronger westerly component. Interestingly, the western low pressure systems in the two longest events were associated with named winter storms (Isaiah and Ruth, respectively). In fact, 12 out of 16 named winter storms that impacted the East Coast were also associated with high shear events giving credence to the idea that strong low pressure systems over the CONUS
255 may produce the synoptic setup required for these offshore high shear events. Expanding to consider the 25 longest events (averaging 19 hours in duration) shows that only 12 exhibit this synoptic structure. This implies that while it is common in the longest events in this area, it may not be a good characterization of all events including those with a much shorter duration.

Lastly, many of the events end around the time of frontal passages as depicted in Fig. 14c. This can be seen in Fig. 8 (event-02,b) where a sharp drop in temperature (bottom panel) coincides with a drastic decrease in shear across the rotor plane
260 (middle panel). Not shown is the wind shift from south-southwesterly to west-northwesterly as would be expected during frontal passage. This results in colder, well-mixed air advecting over the relatively warmer sea surface temperatures and breaks up the stable conditions favorable for generating high shear. On the other hand, the majority of events – such as the event shown in Fig. 8 (event-02, a-c) – end well after frontal passage or have no clear synoptic event that can be attributed to the demise of the high shear. Of the 25 longest events, seven show the ends attributed to frontal passage (one warm front, six cold fronts),
265 however, five of these events are within the ten longest duration events. While this is clearly not applicable to the majority of events, many events, especially those that are around six hours or less in duration, are difficult to determine how the event ends as the synoptic charts are output at six hour intervals. Other noticeable features that were seen in the synoptic charts around the time an event ended were stationary fronts or shortwave troughs (which are commonly associated with changes in wind direction but no, or slight, changes in temperature). Additionally, some events are considered to have “began” or “ended”
270 erroneously due to missing data either before or after the event, respectively. In these cases, it is not possible to determine the physical process that produced or destroyed the high shear event.

There are no clear synoptic differences between the VLLJ events and monotonic shear events. This may be due to the limited observational height where jet noses above 180 m cannot be determined. It is possible that some events that are not considered VLLJs are, in fact, LLJs with noses above 180 m. Additionally, it is possible that only subtle differences in the air temperature,
275 wind speed, and/or wind direction are able to augment the wind profile such that an LLJ nose develops, or doesn't develop, below 180 m.

For the event days that did not display the setup illustrated in Fig. 14 (roughly one quarter of event days), 13% displayed synoptic conditions with a surface high pressure system over the mid-Atlantic region. A similar synoptic environment is found in a case study within (Nunalee and Basu, 2014) where daily low-level jets formed in coastal New Jersey under an area of
280 high pressure centered over the mid-Atlantic states. Additionally, one event occurred as Tropical Storm Arthur approached the lidars from the south off the coast of South Carolina and moved north-northeast. Wind directions, in this case, were from almost directly east, however, air temperatures became warmer than the sea surface temperature as the high shear event began. From this, it becomes apparent that warm air advection over relatively colder water is an essential ingredient to the formation of these high shear events that is typically caused by flow with a large southerly component.

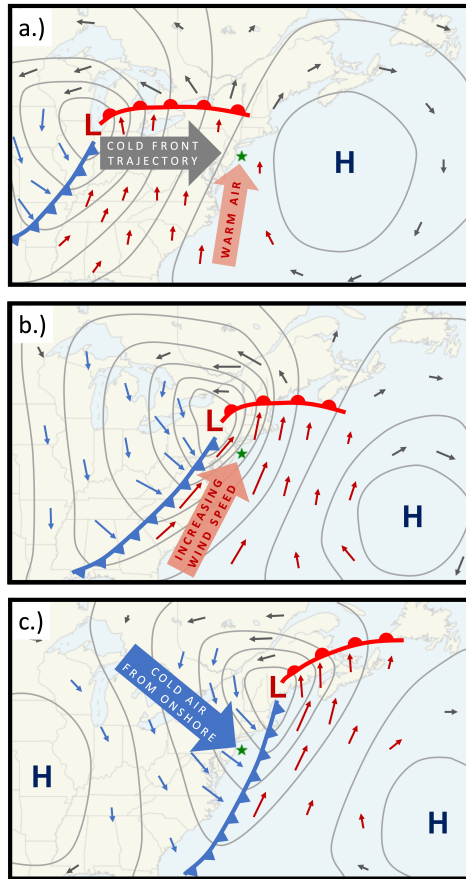


Figure 14. A simplified schematic of the synoptic conditions for high shear events at the beginning (a), during (b), and as the event ends (c). Grey lines represent theoretical isobars, arrows represent typical wind directions, speed, and relative air temperature to the floating lidars (green star), L and H represent low and high pressure centers, respectively.

285 5 Conclusions

This study has revealed the frequent occurrence of extreme high shear events in US mid-Atlantic offshore wind lease areas. These events were characterized based on data from two floating lidars recently deployed by NYSERDA. We identified approximately 100 high-shear events over a year, with some events lasting up to three days. The magnitude of these events was striking, with maximum and mean hub-height wind speeds of 33 m/s and 16 m/s, respectively, and maximum and mean of
290 power-law wind shear exponent across the rotor of 0.82 and 0.28, respectively. These values are substantially higher than 0.2, the number proposed in the design standards to identify extreme shear conditions relevant to turbine operation IEC (2019). It is clear that once wind farms are built in these areas, these extreme events will have substantial effects on wind turbine power generation and structural response.



Fortunately, these extreme events seem to be fairly predictable. We found that their occurrences were strongly associated
295 with a positive air-sea temperature difference, which occurs when warmer air from the southwest flows over the colder waters
of the mid-Atlantic, thereby inducing a stable stratification. These events largely occurred in spring and early summer when
the air-sea temperature difference was greatest, and very seldom in fall and winter when the air-sea temperature difference is
the lowest. The atmospheric conditions leading to these high-shear events is consistent with previous work (Colle and Novak,
2010; Zhang et al., 2006), which had attributed offshore LLJs closer to the coast. The measurements analyzed herein reveal
300 that the high shear and jets persist further from the coast, at offshore distances where wind development is planned.

The high-shear events were characterized by low turbulence: $\sim 4.7\%$ TI on average, in contrast to 8.1% when all the data
are considered. We note, however, that the accuracy of TI measurements from the floating lidars was not assessed in this study.
Future work examining such accuracy would be valuable, provided of course that high frequency wind speed measurement by
the floating lidar is made available.

305 The VLLJ events were especially notable, given their dominant nose heights of 80 m and 100 m and the impact such profiles
will have on turbine power generation. Although these events were fairly infrequent, this fact likely has more to do with the
upper limit of 200 m from the lidar measurements. Had measurements been available above this height, it is likely that many
of the identified monotonic shear events may actually be LLJs with noses above 200 m. Given increasing wind turbine hub
heights and rotor diameters (e.g., the IEC 15-MW reference turbine with blade tips extending up to 300 m), further analysis of
310 LLJs above 200 m is warranted.

In identifying these events, we relied on the wind speed gradient, $\Delta U/\Delta z$, rather than the industry standard power law expo-
nent, α (IEC, 2019). The α parameter is non-dimensional and does not consider the magnitude of wind speeds. Consequently,
we found that extreme wind shear events could have low values of α while, conversely, low magnitude wind speed events could
have high values of α . These results suggest revisiting the standard use of α in turbine design standards and the consideration
315 of alternative parameters such as $\Delta U/\Delta z$.

The public availability of floating lidar data was crucial for this analysis. Although many floating lidars are currently de-
ployed in U.S. offshore wind areas, most data are kept confidential and not available for these types of analyses. Moving
forward, future availability of additional floating lidars will be valuable in further characterizing the regional differences in
extreme wind shear events and how they depend on factors such as proximity to the coastline, latitude, and seasonal changes
320 in SST. Furthermore, these floating lidars will become vital in validating NWP models in offshore wind areas, especially their
ability to accurately predict these high shear events.

Author contributions. MD led the data analysis with significant contributions from PD and PH. MD wrote the article with equal contributions
from MO, PD and PH. NB downloaded and processed the lidar data.

Competing interests. The authors declare that they have no conflict of interest.



325 *Acknowledgements.* This work was authored by the National Renewable Energy Laboratory, operated by Alliance for Sustainable Energy,
LLC, for the U.S. Department of Energy (DOE). Funding for this work was provided by the Bureau for Ocean Energy Management under
Contract Number IAG-19-02122-1. The views expressed in the article do not necessarily represent the views of the DOE or the U.S. Gov-
ernment. The U.S. Government retains and the publisher, by accepting the article for publication, acknowledges that the U.S. Government
retains a nonexclusive, paid-up, irrevocable, worldwide license to publish or reproduce the published form of this work, or allow others to do
330 so, for U.S. Government purposes.



References

- IEC 61400-1:2019-02 (Fourth Edition): Wind energy generation systems – Part 1: Design Requirements, 2019.
- Archer, C. L., Colle, B. A., Delle Monache, L., Dvorak, M. J., Lundquist, J., Bailey, B. H., Beaucage, P., Churchfield, M. J., Fitch, A. C., Kosovic, B., Lee, S., Moriarty, P. J., Simao, H., Stevens, R. J. A. M., Veron, D., and Zack, J.: Meteorology for Coastal/Offshore Wind Energy in the United States: Recommendations and Research Needs for the Next 10 Years: , Bulletin of the American Meteorological Society, 95, 515–519, <https://doi.org/10.1175/BAMS-D-13-00108.1>, <https://doi.org/10.1175/BAMS-D-13-00108.1>, 2014.
- 335 Archer, C. L., Colle, B. A., Veron, D. L., Veron, F., and Sienkiewicz, M. J.: On the predominance of unstable atmospheric conditions in the marine boundary layer offshore of the U.S. northeastern coast, *Journal of Geophysical Research: Atmospheres*, 121, 8869–8885, <https://doi.org/10.1002/2016JD024896>, <https://agupubs.onlinelibrary.wiley.com/doi/abs/10.1002/2016JD024896>, 2016.
- 340 Baas, P., Bosveld, F. C., Klein Baltink, H., and Holtslag, A. a. M.: A Climatology of Nocturnal Low-Level Jets at Cabauw, *Journal of Applied Meteorology and Climatology*, 48, 1627–1642, <https://doi.org/10.1175/2009JAMC1965.1>, <https://journals.ametsoc.org/doi/full/10.1175/2009JAMC1965.1>, publisher: American Meteorological Society, 2009.
- Bodini, N., Lundquist, J. K., and Kirincich, A.: U.S. East Coast Lidar Measurements Show Offshore Wind Turbines Will Encounter Very Low Atmospheric Turbulence, *Geophysical Research Letters*, 46, 5582–5591, <https://doi.org/10.1029/2019GL082636>, <https://agupubs.onlinelibrary.wiley.com/doi/abs/10.1029/2019GL082636>, 2019.
- 345 BOEM: Outer Continental Shelf Renewable Energy Leases Map Book, Tech. rep., Bureau of Ocean Energy Management, 2018.
- Colle, B. A. and Novak, D. R.: The New York Bight Jet: Climatology and Dynamical Evolution, *Monthly Weather Review*, 138, 2385–2404, <https://doi.org/10.1175/2009MWR3231.1>, <https://doi.org/10.1175/2009MWR3231.1>, 2010.
- Colle, B. A., Sienkiewicz, M. J., Archer, C., Veron, D., Veron, F., Kempton, W., and Mak, J. E.: Improving the Mapping and Prediction of Offshore Wind Resources (IMPOWR): Experimental Overview and First Results, *Bulletin of the American Meteorological Society*, 97, 1377–1390, <https://doi.org/10.1175/BAMS-D-14-00253.1>, <https://doi.org/10.1175/BAMS-D-14-00253.1>, 2016.
- 350 DNVGL: OceanTech Services/DNV GL under contract to NYSERDA, Tech. rep., <https://oswbuoysny.resourcepanorama.dnvgl.com/download/f67d14ad-07ab-4652-16d2-08d71f257da1>, 2020.
- Gutierrez, W., Araya, G., Basu, S., Ruiz-Columbie, A., and Castillo, L.: Toward Understanding Low Level Jet Climatology over West Texas and its Impact on Wind Energy, *Journal of Physics: Conference Series*, 524, 012008, <https://doi.org/10.1088/1742-6596/524/1/012008>, <http://stacks.iop.org/1742-6596/524/i=1/a=012008>, 2014.
- 355 Gutierrez, W., Araya, G., Kiliyanpilakkil, P., Ruiz-Columbie, A., Tutkun, M., and Castillo, L.: Structural impact assessment of low level jets over wind turbines, *Journal of Renewable and Sustainable Energy*, 8, 023 308, <https://doi.org/10.1063/1.4945359>, <https://aip.scitation.org/doi/abs/10.1063/1.4945359>, 2016.
- 360 Gutierrez, W., Ruiz-Columbie, A., Tutkun, M., and Castillo, L.: Impacts of the low-level jet’s negative wind shear on the wind turbine, *Wind Energy Science*, 2, 533–545, <https://doi.org/https://doi.org/10.5194/wes-2-533-2017>, <https://wes.copernicus.org/articles/2/533/2017/>, publisher: Copernicus GmbH, 2017.
- Gutierrez, W., Ruiz-Columbie, A., Tutkun, M., and Castillo, L.: The structural response of a wind turbine under operating conditions with a low-level jet, *Renewable and Sustainable Energy Reviews*, 108, 380–391, <https://doi.org/10.1016/j.rser.2019.03.058>, <http://www.sciencedirect.com/science/article/pii/S1364032119301984>, 2019.
- 365 Helmis, C. G., Wang, Q., Sgouros, G., Wang, S., and Halios, C.: Investigating the Summertime Low-Level Jet Over the East Coast of the U.S.A.: A Case Study, *Boundary-Layer Meteorology*, 149, 259–276, <https://doi.org/10.1007/s10546-013-9841-y>, 2013.



- Monin, A. and Obukhov, A.: Basic laws of turbulent mixing in the surface layer of the atmosphere, 2009.
- Murphy, P., Lundquist, J. K., and Fleming, P.: How wind speed shear and directional veer affect the power production of a megawatt-scale
370 operational wind turbine, *Wind Energy Science Discussions*, 2019, 1–46, <https://doi.org/10.5194/wes-2019-86>, <https://wes.copernicus.org/preprints/wes-2019-86/>, 2019.
- Musial, W. and Ram, B.: Large-Scale Offshore Wind Power in the United States: Assessment of Opportunities and Barriers, <https://doi.org/10.2172/990101>, <https://digital.library.unt.edu/ark:/67531/metadc1013438/>, library Catalog: digital.library.unt.edu Number: NREL/TP-500-40745 Publisher: National Renewable Energy Laboratory (U.S.), 2010.
- 375 Nunalee, C. G. and Basu, S.: Mesoscale modeling of coastal low-level jets: implications for offshore wind resource estimation, *Wind Energy*, 17, 1199–1216, <https://doi.org/10.1002/we.1628>, <https://onlinelibrary.wiley.com/doi/abs/10.1002/we.1628>, [_eprint: https://onlinelibrary.wiley.com/doi/pdf/10.1002/we.1628](https://onlinelibrary.wiley.com/doi/pdf/10.1002/we.1628), 2014.
- Pichugina, Y. L., Brewer, W. A., Banta, R. M., Choukulkar, A., Clack, C. T. M., Marquis, M. C., McCarty, B. J., Weickmann, A. M., Sandberg, S. P., Marchbanks, R. D., and Hardesty, R. M.: Properties of the offshore low level jet and rotor layer wind shear as measured by scanning
380 Doppler Lidar, *Wind Energy*, 20, 987–1002, <https://doi.org/10.1002/we.2075>, <https://onlinelibrary.wiley.com/doi/abs/10.1002/we.2075>, 2017.
- Poulos, G. S., Blumen, W., Fritts, D. C., Lundquist, J. K., Sun, J., Burns, S. P., Nappo, C., Banta, R., Newsom, R., Cuxart, J., Terradellas, E., Balsley, B., and Jensen, M.: CASES-99: A Comprehensive Investigation of the Stable Nocturnal Boundary Layer, *Bulletin of the American Meteorological Society*, 83, 555–582, [https://doi.org/10.1175/1520-0477\(2002\)083<0555:CACIOT>2.3.CO;2](https://doi.org/10.1175/1520-0477(2002)083<0555:CACIOT>2.3.CO;2), [https://doi.org/10.1175/1520-0477\(2002\)083<0555:CACIOT>2.3.CO;2](https://doi.org/10.1175/1520-0477(2002)083<0555:CACIOT>2.3.CO;2), 2002.
385
- Rose, S., Jaramillo, P., Small, M. J., Grossmann, I., and Apt, J.: Quantifying the hurricane risk to offshore wind turbines, *Proceedings of the National Academy of Sciences*, 109, 3247–3252, <https://doi.org/10.1073/pnas.1111769109>, <https://www.pnas.org/content/109/9/3247>, ISBN: 9781111769109 Publisher: National Academy of Sciences Section: Physical Sciences, 2012.
- Strobach, E., Sparling, L. C., Rabenhorst, S. D., and Demoz, B.: Impact of Inland Terrain on Mid-Atlantic Offshore Wind and
390 Implications for Wind Resource Assessment: A Case Study, *Journal of Applied Meteorology and Climatology*, 57, 777–796, <https://doi.org/10.1175/JAMC-D-17-0143.1>, <https://doi.org/10.1175/JAMC-D-17-0143.1>, 2018.
- Stull, R. B.: *An Introduction to Boundary Layer Meteorology*, Springer, <https://doi.org/https://doi.org/10.1007/978-94-009-3027-8>, 1988.
- Wharton, S. and Lundquist, J. K.: Atmospheric stability affects wind turbine power collection, *Environmental Research Letters*, 7, 014 005, <https://doi.org/10.1088/1748-9326/7/1/014005>, <https://doi.org/10.1088/1748-9326/7/1/014005>, 2012.
- 395 Zhang, D.-L., Zhang, S., and Weaver, S. J.: Low-Level Jets over the Mid-Atlantic States: Warm-Season Climatology and a Case Study, *Journal of Applied Meteorology and Climatology*, 45, 194–209, <http://www.jstor.org/stable/26169887>, 2006.